Asteroid 4179 Toutatis: First Results of the 1992 Radar Imaging Experiment

S. J. Ostro, R. S. Hudson, R. F. Jurgens, K. D. Rosema, 11.11. Campbell,

D. K. Yeomans, J. F. Chandler, J. D. Giorgini, R. Winkler, R. Rose, S. D. Howard,

M. A, Slade, P. Perillat and 1. I. Shapiro

May 1995

S. J. Ostro, R. F. Jurgens, K. D. Rosema, D. K. Yeomans, J. D. Giorgini, R. Winkler, R. Rose, S. D. Howard, and M. A. Slade are at the Jet Propulsion Laboratory, California Institute of Technology, Pasadena, CA 91109-8099 USA. R. S. Hudson is at the School of Electrical Engineering and Computer Science, Washington State University, Pullman, WA 99164-2752, USA. D. B. Campbell is at the National Astronomy and Ionosphere Center, Space Sciences Bldg., Cornell University, Ithaca, NY 14853-6801, USA, J. F. Chandler and I. I. Shapiro are at the Center for Astrophysics, 60 Garden St. Cambridge,MA02138, USA. P. Perillat is at the Arecibo Observatory, Box 995, Arecibo, PR 00613, USA.

Radar observations of Toutatis on 18 consecutive days during its 1992 close Earth approach provide physical and dynamical information that is unprecedented for an Earth-crossing object. Delay-Doppler images achieve resolutions as fine as 125 ns (19 m In range) and 8.3 mHz (0.15 mm S-l In radial velocity), placing hundreds to thousands of pixels on the asteroid. Toutatis is more than 3 km long, extremely nonconvex, and appears to consist of two structural components in contact, one noticeably larger than the other. The images show craters with diameters ranging from about 100 m to about 600 m. Toutatis has a highly unusual, non-principal-axis spin state with characteristic time scales on the order of several days. The asteroid's orbit has been refined significantly by time-delay measurements that are referenced to the asteroid's center of mass and have fractional precisions of order 10"8.

Earth-orbit-crossing asteroids (ECAS) are of interest for their relationships to meteorites, main-belt asteroids, and comets (1); as the cheapest targets of human or robotic exploration beyond the Earth-Moon system (2); as sources of materials with potential commercial value (3); and as long-term collision hazards (4). About 200 ECAS have been discovered, but the population is thought to include some 1500 larger than one kilometer and some 135,000 larger than 100 m (5), Our knowledge of the physical nature of these objects is limited by their small angular sizes when viewed from Earth (typical] y <<1 arcsec), which makes plane-of-sky resolution difficult for optical telescopes. However, radar measurements of the distribution of echo power in time delay (range) and Doppler frequency (radial velocity) can synthesize images

of these objects. This paper reports delay-Doppler imaging of the ECA 4179 Toutatis with areal resolutions - 100 times finer than previously obtained (6) for any ECA. Our images reveal an object with startling physical characteristics.

Asteroid 4179 Toutatis (formerly 1989 AC) was discovered by C. Pollas on 4 Jan 1989 at Caussols, France (7). The asteroid's orbit has the lowest inclination to the ecliptic plane of any known ECA. It is in a 3:1 mean-motion resonance with Jupiter (8) that serves as a dynamical pathway from main-belt orbits to Earth-crossing orbits on time scales of 10^6 y. Toutatis may have the most chaotic orbit studied to date (9), a consequence of the asteroid's frequent close approaches to Earth.

Toutatis' approach to within 0.024 AU (9.4 lunar distances) on 8 Dec 1992 presented an unprecedented opportunity for radar investigation of a small body. Optical constraints on its physical properties [size **-2.7 km,** slow rotation, S class (10)] led us to expect echoes an order of magnitude stronger than in previous asteroid/con~et radar experiments. The southerly declinations near closest approach made conditions more favorable for the fully steerable Goldstone Radar in California than for the Arecibo Observatory in Puerto Rico. Images placing hundreds to thousands of resolution cells on Toutatis were obtained at Goldstone daily during Dec. 2-18 and at Arecibo daily during Dec. 14-19. Here we describe the observations, present images from each date, and report our principal results.

Observations. We used binary-phase-coded waveforms (1 1) that provide a time resolution At equal to the temporal extent of each code element, a range resolution equal to Δt times half the speed of light, and a frequency resolution

$$\Delta f = 1/(\mathrm{RP} \times \mathrm{NCOH} \times \mathrm{LFFT}) = 1/T\mathrm{COH} \qquad (1)$$

where the code repetition period RP equals A? times the number of elements in the code (255 for Gold stone, 8191 for Arecibo) and NCOH is the numbei of successive, RP-long time series of decoded voltage samples that are coherently summed pi ior to spectral analysis with a Fast Fourier transform of length LFFT (256 for Goldstone, 2048 for Arecibo). A power spectral estimate for each delay "bin" is obtained from coherent analysis of TCOH seconds of data. We refer to such an image as one look. Spectral estimation noise is chi-square distributed and the fractional r.m.s. fluctuation in each pixel of a sum of N images is $N^{-1/2}$. (For our images, background receiver noise is much weaker than echo "self noise.") Thus, fine frequency resolution requires a long coherence time TCOH and low noise requires incoherent summation of many looks. However, long integrations are undesirable if the resolution is degraded by smearing from either the target's rotation or from its translational motion with respect to the delay-Doppler prediction ephemeris, which is used to drift the sampling time base to maintain co-registration of echoes from any given range bin and to tune the receiver's local oscillator to the Doppler-shifted echo. The Doppler-prediction error $\Delta\nu_{eph}$ at a given transmitter frequency F_{TX} defines the rate of change of the delay-prediction error $\Delta\tau_{eph}$ and hence the rate of delay smearing:

$$d\Delta\tau_{eph}(t) / dt = - \Delta\nu_{eph}(t) / F_{TX} \qquad (2)$$

At Goldstone, our observations progressed through four generations of increasingly accurate ephemerides (Table 1). This paper focuses on multilook sums of "low-resolution" images (Δt = 500 ns, Δf = 100 mHz, TCOH = 10s) that suffered negligibly from translational or rotational smearing. We also present multilook sums of selected "medium-resolution" images

(At = 125 ns, Δf = 33 to 138 mHz, TCOH = 30 to 7 s); for these, translational motion is significant, but estimation of $\Delta\nu_{eph}(t)$ has allowed reasonably accurate look-to-look co-registration of the echoes. Our highest-resolution images (Δt = 1.25 ns, Δf = 8 to 17 mHz, TCOH = 121 to 60s) require both rotational and translational motion compensation and will be reported later.

All Goldstone observations used the 70-m antenna, DSS-14, for transmission, Prior to Dec. 3 and after Dec. 14, and in most low-resolution observations, we transmitted for a duration close to the echo's roundtrip time delay (RTT) and then received the echoes for a somewhat shorter duration. The transmit and receive configurations operate with two different feed horns and switching between them requires rotation of the antenna's subreflector, a process that takes 14 to 25 s. Near closest approach, with the RTT ~ 24s, single-antenna observations would leave $\leq$ 10s for signal integration, precluding frequency resolution finer than 0.1 Hz. Since the echo bandwidth was typically $\leq$ 2 Hz and much finer resolution was desirable, most high-resolution Goldstone imaging was done bistatically, transmitting continuously from DSS-14 and receiving at DSS-13, a 34-m antenna 22 km away.

The day-by-day progression of our experiment was strongly conditioned by technical experience with Goldstone's bistatic configuration and real-time display, both of which were "broken in" during these observations, Daily setup decisions were based on the trade-offs among spatial resolution, orientational resolution, and noise, in the context of the echoes' offset from the Doppler prediction ephemerides (Table 1). On the first observation date, Nov. 27, echoes in the same circular polarization as transmitted (the SC sense) were seen to be several times weaker than those received in the opposite circular (OC) polarization, SC low-resolution images from the first week of December were similar to, but weaker than, the.ir OC counterparts, so we received OC echoes exclusively after Dec. 8 at Golds{ one and in almost all our Arecibo runs.

Arecibo's transmitter frequency is 3.58 times lower than Goldstone's, so one look at a given radial-velocity resolution requires a correspondingly longer coherent integration at Arecibo. However, all Arecibo observations were monostatic, and this fact plus Arecibo's smaller hour-angle window limited coherent and incoherent integration times. Nonetheless, the Arecibo observations provided the highest-resolution images after Dec. 16 and our only data on Dec. 19.

images. Figure 1 shows Goldstone 0.5-μs images and Arecibo 0.2-μs images. These images are geometrically very different from optical pictures. Constant-Doppler planes are parallel to both the line of sight (LOS) and the target's apparent spin vector, and constant-delay planes are normal to the 1.0S. These two orthogonal sets of planes cut the target into rectangular cells much as one dices a potato to make french fries. Our images show the sum of all the echo power in each cell, Beyond the leading edge, where the surface-to-image mapping is typically one-to-one, each cell can capture echoes from surface regions on either side of the apparent equator, so the mapping is potentially two-to-one or even many-to-one.

For a rigid body whose center of mass (COM) is at a constant distance from the radar, the Doppler frequency of the echo from a surface point **r** with respect to the COM is

$$\nu = (\mathbf{W}_{app} \times \mathbf{r}) \cdot \mathbf{e} / (\lambda/2) \qquad (3)$$

where the unit vector e points from the COM to the radar and we have ignored parallax and second-order terms. The target's apparent spin vector W_{app} satisfies

$$w_{app} = w + \mathbf{W}_{sky} \qquad (4)$$

where W is the intrinsic spin vector and $\mathbf{W}_{sky}$ is the contribution from the plane-of-sky (POS) motion of the target. The km/Hz conversion factors can be written

Goldstone: km/Hz:= 87.2 / $|\mathbf{W}_{app} \times \mathbf{e}|$ (5)

$$= 87.2/(1\ \mathbf{W}_{app}| \cos \delta)$$

$$= P / (4.13 \cos \delta)$$

Arecibo: km/Hz = 312/ $|\mathbf{W}_{app} \times \mathbf{e}|$ (6)

$$= 3\,12/ (1\ \mathbf{W}_{app}| \cos \delta)$$

$$= P / (1.15 \cos \delta)$$

where spin rates are in degrees per day, P = 3600/1 $\mathbf{W}_{app}|$ is the instantaneous, apparent spin period in days, and δ is the instantaneous, apparent, asteroid-centered declination of the radar. The following discussion focuses on the Goldstone image sequence.

The echo dispersion ranges from’7 to 21 μs in delay [1.0 to 3.1 km in range (12)] and from 0.4 to 2.2 Hz in Doppler. The distribution of echo power is extremely bimodal in most frames (two lobes are perceptible even on Dec. 3,7, 14, and 17, when they are at similar distances from the radar and their echoes overlap), indicating a prominent bifurcation in the asteroid’s shape. On Dec. 5-6, the lobes’ central frequencies are similar and the large lobe is between the radar and the

small lobe. No eclipse of the small lobe is evident, so a POS view of the asteroid would be expected to show both lobes. A similar statement applies to Dec. 15-16. However, during Dec. 10-12, when the small lobe is closer to the radar, the large lobe's terminator extends several microseconds further at frequencies not shared by the small lobe than it does at frequencies containing echoes from both lobes. This pattern suggests partial occultation of the large lobe by the small lobe. The Dec. 11 frame also shows the asteroid's greatest delay depth. Thus it appears that the lobe-lobe line coincides approximately with the asteroid's longest dimension and that both are closer to the LOS on Dec. 11 than on any other date. That frame shows a gap of- 0.3 km between the lobes' range distributions, indicating negative relief between the smaller lobe's terminator and the larger lobe's leading edge. The delay dispersions of the two components' echoes place lower bounds of 0.9 and 1.9 km on their maximum overall dimensions, but to decipher their shapes and that of the asteroid as a whole we must know the Hz-to-km conversion factor (i.e., I $\mathbf{W}_{app}$ *X cl)* as a function of time.

Extraordinary rotation. The asteroid's hour-to-hour rotational motion was barely perceptible in the real-time displays, but day-to-day changes in the orientation of the line connecting the two lobes were readily seen. During the first few days, the motion of the lobe-lobe line and naive application of Eq. 5 suggested a rotation period between 4 and 5 days (13) and a view closer to equatorial than pole-on. For example, since the asteroid's typical overall dimension appears to be about 2 km and its typical bandwidth is about 2 Hz over most of the imaging sequence, one might gather from Eq. 5 that the POS component $|\mathbf{W}_{app} \times \mathbf{e}|$ of $\mathbf{W}_{app}$ was roughly 90°/day. (Note from Table 1 that the asteroid's POS motion $|\mathbf{W}_{sky}|$ was much slower and therefore has a negligible effect on the delay-Doppler signature over most of the imaging sequence.)

However, as the experiment progressed, it became increasingly difficult to identify any constant value for W that was consistent with the evolution of the delay-Doppler signature, and by the end of the experiment we realized that our premise of principal-axis rotation was incorrect. According to force-free rigid-body dynamics, if the angular momentum vector I. is not aligned with a principal axis, the body-fixed inertia ellipsoid wil 1 freely precess about L while W executes a periodic motion in the body, its direction defining a closed curve on the inertia ellipsoid (14). Let the principal axes xl, X_2, x_3 correspond to moments of inertia $I_1 > I_2 > I_3$. Rotation is stable only about x_1 or X_3. Convergence of L with x_1 generally will occur whenever energy dissipation is taking place in a quasi-rigid body (15); lightcurves overwhelming y support the conclusion that such rotation is predominant among the asteroids (16). In contrast, for Toutatis, the lobes always overlap in frequency, even on Dec. 3, 7 and 14, when they are at similar ranges, so we never see $\mathbf{W}_{app}$ normal to the longest dimension. Since $|\mathbf{W}_{sky}|$ is very small compared to $|\mathbf{W}_{app} \times \mathbf{e}|$, we conclude that W is not normal to the asteroid's longest dimension; in fact, most of the frames suggest that W is closer to the longest dimension than to its normal. Whereas this circumstance suggests either non-principal axis rotation or very unusual physical properties, it does not in itself preclude principal axis rotation, since the asteroid's shape and internal density distribution (and hence the inertia ellipsoid's shape and body-fixed orientation) are unknown.

However, other aspects of the image sequence do demonstrate variation of W, thereby establishing non-principal-axis rotation. For example, consider the implications of the striking similarity of the Dec. 2 and Dec. 13 frames, for which c differs by 1100. If W were constant in body-fixed and inertial frames, that pattern would require δ to be similar on each date, but that possibility is ruled out by the bandwidth collapse on Dec. 11, only 13° from the Dec. 13 position, Also note that the Dec. 11 bandwidth is about half of that in either adjacent frame, although the

asteroid's direction was changing by only 7° from day to day. If all other factors were equal and if W were constant in body-fixed and inertial frames, then the twofold change in bandwidth within a 7° excursion in e would imply that W_{app} was about 7° from the LOS on Dec. 11. If we take 2 km as an upper bound on the asteroid's POS extent normal to W_{app} during these dates, then $|W_{app} \times \hat{e}|$ was at least 170/d on Dec. 11 and twice that on the adjacent dates. Since $|W_{sky}|$ was only 70/d, the bandwidth collapse on Dec. 11 must be due primarily to the collapse of $|W \times \hat{c}|$, which in turn could mean either that $|W|$ was much smaller than on dates far from Dec. 11 (i.e., W's magnitude varies) or that W was very close to the lobe-lobe line on Dec. 11. However, since the lobe-lobe line itself is seen rotating from day to day through most of the rest of the image sequence, the latter possibility would mean that W's body-fixed direction varies. We conclude that the image sequence cannot be reconciled with a spin vector that is constant in inertial and body-fixed frames.

Burns (17) argued that for plausible asteroid shapes in non-principal-axis rotation, the time scale for precession of the inertia ellipsoid about L will be within a factor of 10 of the rotation time scale. Periods on the order of days are suggested by visual inspection of Fig. 1 and the above analyses (18), but accurate determination of the asteroid's rotation clearly requires inversion of the image sequence with a realistic physical model.

Model-based dilation and de-smearing of images. Hudson and Ostro (19) have carried out such an inversion on the low-resolution Goldstone images and the Dec. 19 Arecibo image, by modeling the asteroid's shape and inertia tensor, their orientation with respect to each other, initial conditions for the asteroid's spin and orientation, the radar scattering properties of the surface, and the location of the COM in each frame. The model-based ephemeris corrections $\Delta\tau_{eph}$ and $\Delta\nu_{eph}$ (Table 1) yield delay-Doppler astrometry (Table 2) that has been used to refine Toutatis'

orbit (Table 3). The model-based Doppler corrections also have been used to de-smear our medium-resolution Goldstone images, which in Fig. 2 have been dilated according to km/Hz conversion factors (Table 1) from the model solution for W(t). The leading edges show a degree of angularity comparable to that seen in Galileo images of the much larger asteroid 243 Ida (20). The clearest images in Fig. 2 reveal numerous surface depressions. Many of them, including the more than one dozen oval-shaped features in the Dec. 8 frame, probably are impact craters. The diameters of those features range from less than 100 m to more than 600 m. Toutatis' irregular, cratered shape and unusual rotation undoubtedly record a rich collisional history. Precise definition of the surface relief is expected from global inversion of the medium- and high-resolution images.

Conclusions. Given the intensity and outcome of the Toutatis investigations, it maybe appropriate to think of our experiment as a flyby of Toutatis by an Earthborne package of radar sensors. Toutatis will be observable by radar during its close approaches in 1996 (0.035 AU), 2000 (0.074 AU), and 2004 [0.01 1 AU, or four lunar distances, the closest predicted approach of any asteroid or comet to Earth during the next 60 years (2 l)]. It should be possible to obtain images providing decameter resolution during each of these "fly bys. "

Delay-Doppler radar is likely to be the primary telescopic source of information about ECA physical properties for the foreseeable future. During the next 20 years, there are about 30 opportunities for Arecibo and/or Goldstone to image one of the known ECAS at high resolution (-1000 pixels on the target) and about 100 opportunities at lower (-100-pixel) resolution. Improvements in optical search programs (22) could increase the frequency of opportunities by more than an order of magnitude.

REFERENCESAND NOTES

1. G. W. Wetherill and C. R. Chapman, in *Meteorites and the Early Solar System,* J. F. Kerridge and M. S. Matthews, Eds. (Univ. of Arizona Press, Tucson, 1988), pp. 35-67.
2. T. D. Jones *et al., in Hazards Due to Comets and Asteroids, T.* Gehrels, Ed. (Univ. of Arizona Press, Tucson, 1994), pp. 683-708.
3. W. K. Hartmann and A. Sokolov, in *Hazards Due to Comets and Asteroids,* T. Gehrels, Ed. (Univ. of Arizona Press, Tucson, 1994), pp. 1213-1224; J. S. Lewis, M. S. Matthews, M. L. Guerrieri, Eds., *Resources of Near-earth Space* (Univ. of Arizona Press, Tucson, 1993).
4. D. Morrison, C. R. Chapman, P. Slovic, in *Hazards Due to Comets and Asteroids,* T. Gehrels, Ed. (Univ. of Arizona Press, Tucson, 1994), pp. 59-91.
5. D. Rabinowitz, E. Bowell, E. Shoemaker, K. Muinonen, in *Hazards Due to Comets and Asteroids,* T. Gehrels, Ed. (Univ. of Arizona Press, Tucson, 1994), pp. 285-312.
6. S. J. Ostro *et al., Science 248, 1523 (1990).*
7. J.-L. Heudier 1989, *IAU Circular No. 4701 (1989); Minor Planet Circular No. 15061 (1989).*
8. B. G. Marsden, *IAU Circular No. 4715 (1989);* A. M. Milani, M. Carpino, G. Hahn, A. M. Nobili, *Icarus* 78,212.
9. A. L. Whipple and P. J. Shelus, *Icarus* J 05,408 (1993).
10. D. J. Tholen, *Bull. Amer. Astr. Sot. 24,934 (1992).*
11. *G.* H. Pettengill, in *Radar Handbook,* M. I. Skolnik, Ed. (McGraw Hill, New York, 1970), chap. 33; S. J. Ostro, *Reviews of Modern Physics 65,* 1235 (1993).
12. The echo's range dispersion places a lower bound on the target's LOS extent.

13. Almost all measured ECA rotation periods are between 0.1 and 1.0 d; R. Chapman, A. W. Harris, R, P, Binzel, in *Hazards Due to Comets and Asteroids,* T. Gehrels, Ed. (Univ. of Arizona Press, Tucson, 1994), pp. 537-549.

14. L. D. Landau and E. M. Lifshitz, *Mechanics* (Pergamon Press, New York, 1976), pp. 114-120; H. Goldstein, *Classical Mechanics* (Addison-Wesley, London, 1950), pp. 143-163.

15. K. H. Prendergast, *Astron. J.* **63,412 (1958);** R. Pringle, Jr., *AIAA J. 4, 1395-1404 (1966)* and historical references therein.

16. A. W. Harris, *Icarus* **107,209 (1994).**

17. J. A. Burns, in *Physical Studies of Minor Planets*, T. Gehrels, Ed. (Univ. of Arizona, Tucson, 197 1), pp. 257-2.62.

18. Harris (16) has pointed out that for small asteroids rotating that slowly, the time scale for damping non-principal-axis rotation is longer than the age of the solar system. See also J. A. Burns and V. S. Safranov, Mon. *Not. R. Astr. Sot.* **165,403 (1973).**

19. R. S. Hudson and S. J. Ostro, Science, submitted for publication (1995).

20. M. J. S. Belton *et al., Science 265, 1543 (1994).*

21. D. K. Yeomans and P. W. Chodas, in *Hazards Due to Comets and Asteroids,* T. Gehrels, Ed. (Univ. of Arizona Press, Tucson, 1994) pp. 241-258.

22. E. Bowell and K. Muinonen, in *Hazards Duc to Comets and Asteroids*, T. Gehrels, Ed. (Univ. of Arizona Press, Tucson, 1994), pp. 149-197.

23. We thank the Goldstone and Arecibo technical staffs for their support of these observations. Part of this research was conducted at the Jet Propulsion Laboratory, California Institute of Technology, under contract with the National Aeronautics and Space Administration (NASA). The Arecibo observatory is part of the National

Astronomy and Ionosphere Center, which is operated by the Cornell University under a cooperative agreement with the national Science Foundation and with support from NASA. Work at Washington State University and the Center for Astrophysics was supported in part by NASA.

FIGURE CAPTIONS

Fig. 1. Toutatis radar images. Goldstone low-resolution images from Dec. 2- Dec. 18 (top three rows) and Arecibo images from Dec. 14- Dec. 19 (bottom row) are plotted with time delay increasing toward the bottom and Doppler frequency increasing toward the left, so the rotation is clockwise. On the vertical sides, ticks are separated by 2 μs. Two horizontal sides have ticks separated by 1 Hz for Goldstone and 0.28 Hz for Arecibo; those intervals correspond to a radial velocity of 18 mm s^{-1}. Gray scales were designed to show the extent of the delay-Doppler distributions and as much brightness contrast as possible. See Table 1.

Fig. *2.* Medium-resolution Goldstone images of Toutatis from the indicated December dates, dilated according to km/Hz conversion factors predicted by the Hudson-Ostro (1995) model for the asteroid's spin state. The geometry is the same as in Fig. 1. Perimeter ticks are spaced by 1 km. Gray scales were designed to show as much brightness contrast as possible. See Table 1.

Table 1. Data files corresponding to images in Figs. 1 and 2. Goldstone (85 IO-MHZ, 3.5-cm) file designations are the day of year followed by a two-digit index; designations for bistatic observations are in italics. For each file we list the delay resolution&, the Doppler resolution Δf and its radial velocity equivalent V_{rad}, the UTC receive interval, the number of looks summed, the km/Hz conversion factor from the Hudson-Ostro (1995) model, the meter equivalents of Δt and Δf, $|W_{sky}|$, the asteroid's right ascension and declination, the echo's roundtrip time delay, and the calculation date for the orbit used to prepare the delay-Doppler ephemeris. For the images in Fig. 1, we list the model-based ephemeris corrections $\Delta\tau_{eph}$ and $\Delta\nu_{eph}$. For Arecibo (2380-MHz, 13-cm) images, the processing technique introduced high correlation between adjacent frequency cells.

Date	File	Δt (ns)	Δf (mHz)	V_{rad} (mm s^{-1})	start - stop (hh:mm)	looks	km/Hz	m/Δf x m/Δt	$\lvert W_{sky}\rvert$ (°/d)	RA	Dec	RTT (s)	Orbit Date	$\Delta\nu_{eph}$ (Hz)	$\Delta\tau_{eph}$ (us)
Goldstone															
2	33707	500	100	1.76	21:29-21:45	7	0.96	96 x 75	5.3	262°	-32°	42	Nov 27	-15.746	-2009.686
3	33804	500	100	1.76	19:12-19:40	1 4	0.86	86 x 75	6.7	256°	-33°	38	Dec 2	-1.150	20.626
4	33904	500	100	1.76	18:02-18:22	1 4	0.85	85 X 75	8.6	248°	-33°	33	Dec 2	-8.045	74.804
5	34003	500	100	1.76	17:09-17:42	1 8	0.89	89 x 75	11.0	237°	-33°	29	Dec 4	1.029	76.588
5	34006	125	83	1.47	18:38-19:11	2 2	0.89	74 x 19	11.2	236°	-32°	29	Dec 4		
6	*34104*	500	100	1.76	16:35-16:50	7 6	0.95	95 x 75	13.6	223°	-31°	26	Dec 4	3.066	49.580
6	34107	125	83	1.47	17:18-17:39	104	0.95	79 x 19	13.7	223°	-31°	26	Dec 4		

7	*34204*	*500*	*100*	1.76	17:03-17:44	8 3	1.12	112 x 75	15.6	207°	-27°	24	Dec	4	-2.576	*32.398*
8	34304	500	100	1.76	14:18-14:58	2 5	1.37	137 x 75	15.6	194°	-21°	24	Dec	7	-0.970	*19.385*
8	34307	125	33	**0.58**	16:07-17:02	106	1.39	46X19	15.6	193°	-21°	24	Dec	7		
9	**34402**	**500**	100	1.76	17:25-17:41	9	1.77	1'7'7 x '75	13.5	179°	-14°	26	Dec	7	-0,049	*28.203*
9	34403	125	33	0.58	17:47-18:01	2 5	1.78	59 x 19	13.4	179°	-14°	26	Dec	7		
10	34503	500	100	1.76	16:51-16:59	6	2.88	287 x 75	10.9	169°	-8°	29	Dec	7	0.994	*23.054*
10	34504	125	33	0.58	17:03-17:40	7 2	2.90	96 x 19	10.9	169°	-8°	29	Dec	7		
11	34603	500	100	1.76	09:21-09:56	1 5	4.77	476 x 75	9.1	163°	-4°	32	Dec	7	0.765	*17.114*
11	34605	125	33	0.58	10:02-11:04	106	4.85	161 x *19*	9.1	163°	-4°	32	Dec	7		
12	34703	500	100	1.76	09:06-09:36	1 8	2.13	*213* x 75	7.1	157°	0°	36	Dec	7	-0.305	*15.231*
13	34803	500	100	1.76	08 :02-08:23	25	1.19	119 x 75	5.5	152°	3°	41	Dec	7	-0.433	20.577
13	34805	125	33	0.58	08:32-09:57	162	1.17	39 x 19	5.5	152°	3°	41	Dec	7		
14	34903	500	100	1.76	07:36-08:09	3 0	0.93	86 x 75	4.4	148°	6°	46	Dec	'i	0.449	*21.152*
14	*34906*	125	33	0.58	08:32-09:26	9 9	0.92	30 x 19	4.4	148°	6°	46	Dec	'i		
15	35002	500	100	1.76	07:35-07:53	2 9	0.86	86 x 75	3.5	144°	8°	52	Dec	7	0.866	*14.100*
16	35104	500	100	1.76	07:01-07:14	1 8	0.86	86 x 75	2.9	142°	9°	57	Dec	7	-0.583	*10.643*
17	35204	500	100	1.76	06:39-06:53	2 7	0.90	86 x 75	2.4	140°	11°	63	Dec	7	-2.054	*25.794*
18	35304	500	100	1.76	06:21-08:08	151	1.15	86 x 75	2.0	138°	12°	69	Dec	7	-0.818	*45.418*

Arecibo															
14	200	12	0.78	08:19-09:46	3 6	3.27	41 x 30	4.4	148°	6°	46	Dec 8			
15	200	12	0.78	07:30-09:23	5 3	3.30	41 x 30	3.5	148°	6°	46	Dec 8			
16	200	12	0.78	07:12-09:21	8	3.08	38 x 30	2.9	148°	6°	46	Dec 8			
17	200	12	0.78	07:03-09:03	5 6	3.23	40 x 30	2.4	140°	11°	63	Dec 8			
18	200	12	0.78	06:54-08:50	4 7	4.09	51 X30	2.1	138°	12°	69	Dec 8			
19	200	12	0.78	06:36-08:42	4 6	5.6'7	70 x 30	1.8	136°	13°	'75	Dec 8	-0.26	-2.72	

Table 2. Goldstone radar astrometric results for Toutatis. Measurements correspond to echoes from the estimated position of the asteroid's center of mass in the Hudson-Ostro (1995) model. Epochs are referred to the instant of reception. For DSS-13 and DSS-14, the reference point is the intersection of the azimuthal and elevation axes. Goldstone's transmitter frequencyis8510 MHz.

UTC epoch (hh:mm)	Antenna(s)	Time delay (s ± μs)	Doppler frequency (Hz ± Hz)
1992 12 02 21:40	14	42.180312122 ± 0.55	523514.760 ± 0.13
1992 12 03 19:30	14	37.450923337? 0.36	494766.0195 0.07
1992 12 04 18:10	14	32.975711079 ± 0.41	443775.7325 0.08
1992 12 05 17:30	14	29.027804001 ± 0.30	362243.9022 0.06
1992 12 06 16:40	14->13	26.056497203 ± 0.23	248335.943 ± 0.04
1992 12 07 17:20	14->13	24.3073057455 0.61	
1992 12 08 14:40	14	24.202819270 ± 0.12	-58758.5872 0.02
1992 12 09 17:30	14	25.938852115A 0.34	-250054.867 ± 0.06
1992 12 10 17:00	14	28.8675658082 0.38	-364551.377 ± 0.07
1992 12 11 09:40	14	31.542082782 ± 0.34	-389322.673 ± 0.05
1992 12 12 09:20	14	35.939781859A 0.32	-450249.232 ± 0.05
1992 12 13 08:10	14	40.664482454 ± 0.41	-487485.645? 0.08
1992 12 14 07:50	14	45.8912875055 0.48	-515942,546? 0.09

1992	12	15	14	51.433656661 ± 0 59	-537151 849 ± 0 11
1992	12	16	14	56.397841703 ± 0.80	55072 983 ± 0 16
1992	12	17	14	62 767761168 ± 0 84	-561924.364 ± 0 16
1992	12	18	14	68 80974112 ± 0.47	57257 338 ± 0 09

Table 3. Orbit of Toutatis. Together with over 400 optical astrometric observations over the interval from 1988 July 12 through 1993 April 18, the astrometric radar data in Table 2 were used to compute an improved orbit for the asteroid. The JPL planetary ephemeris DE 245 was used in the following orbital solution; an independent solution using the CfA ephemeris PEP740 gave a result agreeing to within the stated uncertainties in all the orbital elements. The epoch was selected for its proximity to the next close Earth approach on Nov. 29, 1996 (0.035 AU). The angular orbital elements are referred to the mean ecliptic and equinox of J2000. Conservative 3-standard-deviation uncertainties (in parentheses) are given in units of the last decimal place. Tine weighted rms residuals for the optical, Doppler, and delay observations are respectively 0.83 arc seconds, 0.08'7 Fiz (i.5 mm s^{-1} in radial velocity) and 0.39 μs (59 m in range).

Epoch (TDB)	1996 Nov. 13.0
Perihelion passage time (TDB)	1996 Nov. 11.04640 (2)
Perihelion distance (AU)	0.920615832 (13)
Eccentricity	0.634085830 (5)
Argument of perihelion (deg)	274.45243 (135)
Longitude of ascending node (deg)	128.64567 (135)
Inclination (deg)	0.46751 (1)

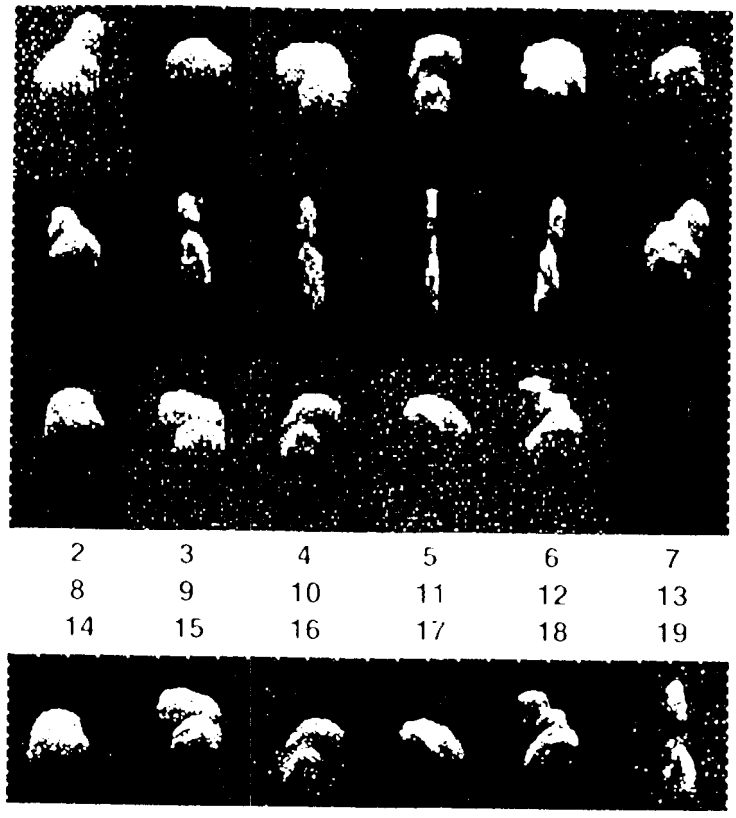

2 3 4 5 6 7
8 9 10 11 12 13
14 15 16 17 18 19

Osuo *et a* Fig. 1

5 *6* *8* *9*
10 11 **13** **14**

Osuo *et al* Fig. 2